The Radiation Budget of the West African Sahel and Its Controls: A Perspective from Observations and Global Climate Models

MARK A. MILLER, VIRENDRA P. GHATE, AND ROBERT K. ZAHN

Department of Environmental Sciences, Rutgers University, The State University of New Jersey, New Brunswick, New Jersey

(Manuscript received 4 February 2011, in final form 30 March 2012)

ABSTRACT

Continuous measurements of the shortwave (SW), longwave (LW), and net cross-atmosphere radiation flux divergence over the West African Sahel were made during the year 2006 using the Atmospheric Radiation Measurement (ARM) Mobile Facility (AMF) and the Geostationary Earth Radiation Budget (GERB) satellite. Accompanying AMF measurements enabled calculations of the LW, SW, and net top of the atmosphere (TOA) and surface cloud radiative forcing (CRF), which quantifies the radiative effects of cloud cover on the column boundaries. Calculations of the LW, SW, and net cloud radiative effect (CRE), which is the difference between the TOA and surface radiative flux divergences in all-sky and clear-sky conditions, quantify the radiative effects on the column itself. These measurements were compared to predictions in four global climate models (GCMs) used in the Intergovernmental Panel for Climate Change Fourth Assessment Report (IPCC AR4). All four GCMs produced wet and dry seasons, but reproducing the SW column radiative flux divergence was problematic in the GCMs and SW discrepancies translated into discrepancies in the net radiative flux divergence. Computing cloud-related quantities from the measurements produced yearly averages of the SW TOA CRF, surface CRF, and CRE of ~ -19, -83, and 47 W m^{-2}, respectively, and yearly averages of the LW TOA CRF, surface CRF, and CRE of $\sim$39, 37, and 2 W m^{-2}. These quantities were analyzed in two GCMs and compensating errors in the SW and LW clear-sky, cross-atmosphere radiative flux divergence were found to conspire to produce somewhat reasonable predictions of the net clear-sky divergence. Both GCMs underestimated the surface LW and SW CRF and predicted near-zero SW CRE when the measured values were substantially larger ($\sim$70 W m^{-2} maximum).

1. Introduction

A complex monsoon circulation driven by north–south temperature and moisture gradients supplies virtually all rainfall to the West African Sahel. Its precarious geographic location along the tropical margin; its population density, which is roughly equal to that of the northeastern United States; and its economic status combine to increase its vulnerability to climate change. Agrarian societies are dominant across the Sahel and recurrent severe droughts such as those experienced in the 1970s and 1980s caused ‘‘massive losses of agricultural production and livestock; loss of human lives to hunger; malnutrition and diseases; and massive displacements of people and shattered economies’’ (Kandji et al. 2006). A particularly severe drought during 1974 necessitated humanitarian intervention by western countries. Year-to-year precipitation variability during the past 50 years has been linked to excursions in the sea surface temperatures across the tropical Atlantic Ocean (Lamb 1986; Lamb et al. 1986). This known source of year-to-year variability is superimposed upon a mysterious long-term drought of several decades duration. Links between this extended drought and rising sea surface temperatures very likely associated with greenhouse gas accumulation are unknown.

Important drivers of the radiation transfer and the hydrological cycle of the West African Sahel region include the monsoon circulation, biomass burning, and Saharan dust. Monsoonal flow produces a dry season of several months duration (October–May) during which the low-level flow transports hot and dry air from the Sahara Desert into the northern part of the West African Sahel (Fig. 1). Extreme dust outbreaks as a result of lofting in frontal zones are observed during this dry

Corresponding author address: Mark A. Miller, Dept. of Environmental Sciences, Rutgers University, The State University of New Jersey, 14 College Farm Rd., New Brunswick, NJ 08901.
E-mail: m.miller@envsci.rutgers.edu

DOI: 10.1175/JCLI-D-11-00072.1

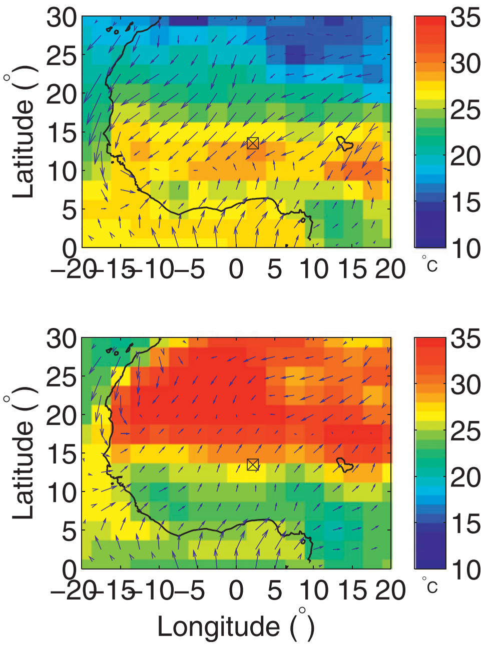

FIG. 1. Surface air temperature (shades) and surface wind vectors for (top) dry season and (bottom) wet season in the northwestern African region as reported by National Centers for Environmental Prediction (NCEP)–National Center for Atmospheric Research (NCAR) reanalysis monthly values for the year 2006. Niamey is shown with a cross within a square.

season (Slingo et al. 2006; Yoshioka et al. 2007). Near-surface winds reverse direction (July–September) and advect cooler and more moist air from the tropical Atlantic into the lowest levels of the atmosphere over the Sahel, undercutting the hot, dry, and dusty air mass above that is associated with the Harmattan trade winds. This advected low-level moisture feeds the precipitating convection observed during this period, leading to its designation as the wet season, and cirrus clouds are observed year round over the Sahel (Kollias et al. 2009).

The West African monsoon is a complex circulation featuring many theorized interactions with other prominent components of the general circulation. Interaction between the Madden–Julian oscillation (MJO) and the West African monsoon has stimulated many modeling and observational studies in recent years (Lavender and Matthews 2009; Pohl et al. 2009 etc.) as has the interaction with the Atlantic intertropical convergence zone (Maloney and Shaman 2008; Gu and Adler 2004 etc.). Postulation that African easterly wave formation is enhanced during the wet season in a manner that affects tropical cyclone formation has also generated interest (Thorncroft and Hoskins 1994; Matthews 2004). A critical feature of the Sahel region is the seasonal north–south migration of the intertropical front (ITF), which marks the leading edge of low-level monsoonal moisture. A recent study shows a strong correlation between the amount of rainfall observed relatively early and late in the wet season and geographic proximity to the ITF, but a significantly weaker correlation with relative location during the core of the wet season (Lélé and Lamb 2010). These intricate interactions present a serious challenge to the global climate models (GCMs) used to simulate the Sahel's future climate and especially its wet season rainfall.

Like many other under-sampled regions, the Sahel suffers from a scarcity of reliable surface observations and a heavy reliance upon satellite radiation measurements to benchmark GCM performance. Even in data-rich areas the cross-atmosphere radiation flux divergence and its controls are rarely measured with the temporal resolution, completeness, and accuracy required to determine how the controls and the radiative fluxes interact. This study overcomes this obstacle using nearly continuous measurements of the broadband radiative fluxes at the TOA and at the surface that were collected by a geostationary satellite positioned above a surface measuring system. Measurements of these boundary radiation fluxes are complemented by simultaneous measurements of the cloud, aerosol, and water vapor structure within the atmospheric column that control radiation throughput. This comprehensive and continuous set of observations permits the radiative heating and cooling effects of clouds upon the atmospheric column and its boundaries to be measured directly at a time scale that is compatible with the cloud life cycle.

This study leverages these unique data using complementary GCM simulations of the past, present, and future climate in the Sahel region from four models presented in the Intergovernmental Panel for Climate Change (IPCC) Fourth Assessment Report (AR4). Forecasting future rainfall in the Sahel is of primary importance, so the study begins with an analysis of the ability of these four models to accurately depict the rainfall and associated hydrological variables observed during a typical year. A principal goal of this study is to gain specific insight into the interplay between clouds and the absorption of SW, LW, and net radiation and to determine how this interplay is represented in GCMs. Measurements of the cross-atmosphere radiative flux divergence over the Sahel lend themselves to the introduction of a new variable defined as the cloud radiative effect (CRE). The exceptional quality and comprehensive nature of these measurements enable the radiative influence of clouds to be isolated from the radiative influence of clear skies at the column boundaries as characterized by the cloud radiative forcing (CRF) and upon the column itself (CRE). Similarly isolated output from two of the four GCMs display intriguing differences in the manner in which cloudy and clear skies are treated in both the LW and SW, and how these differences contribute to the net CRE in the models.

2. Instrumentation

Coincident, semicontinuous, detailed measurements of the LW, SW, and net radiation fluxes at the surface of the West African Sahel and at the TOA were collected using the Atmospheric Radiation Measurement (ARM) Mobile Facility (AMF) and the Meteosat Second Generation (MSG) satellite, which carries two instruments: the Spinning Enhanced Visible and Infrared Imager (SEVIRI) and the Geostationary Earth Radiation Budget (GERB) instrument (Schmetz et al. 2002). Synergistic use of these platforms was a key aspect of the Radiative Divergence using AMF, GERB and African Monsoon Multidisciplinary Analysis (AMMA) Stations (RADAGAST) field campaign, which was based in Niamey, Niger, during 2006 (Miller and Slingo 2007; Slingo et al. 2008, 2009). Structural measurements captured the evolution of the radiatively active components in the atmospheric column at a spatial scale that was relatively fine compared to the coarseness of a typical GCM grid cell. Fortunately, spatial variability in this region is somewhat muted by the remarkably uniform nature of the Sahel landscape, although observed north–south gradients in temperature and moisture may have occasionally caused irresolvable disparities between measurement and model scales. Spatial uncertainties in the surface radiation budget are well characterized in the vicinity of Niamey (Settle et al. 2008) as are the spatial distributions of temperature, maximum relative humidity, and precipitation (Huang et al. 2009; Lélé and Lamb 2010). Spatial distributions of other variables, such as cloud structure, are less certain.

a. AMF instrumentation and data processing

Instrumentation deployed in Niamey as part of the AMF included a cloud-sensing radar, lidars, microwave radiometers, a surface broadband radiometric station, and a surface meteorological station. Vertically pointing cloud radar, known hereafter as the W-band ARM Cloud Radar (WACR), operated at 95-GHz frequency with 6-s and 42-m resolution and had a maximum range of 18 km, enabling it to observe cirrus clouds. A laser ceilometer operating at 905-nm wavelength recorded the lowest cloud-base height that was detected beneath its maximum measurement altitude of 7.5 km every 15 s with 15-m resolution. A higher power laser, known as the micropulse lidar (MPL), operated at 532-nm wavelength with a resolution of 30 m and 30 s and was able to observe cloud-base height and the internal structure of thin cirrus clouds to a height of 18 km when there were no clouds beneath. Data from the WACR, ceilometer, and MPL were combined to determine the cloud boundaries at 6-s resolution (Kollias et al. 2009). Hourly averaged cloud boundaries and cloud fraction as a function of height constitute the characterization of cloud structure in this study. The presence of cloud in the vertical column was estimated for each 42-m layer sampled by the AMF cloud radar and the fraction of each 1-h period occupied by clouds in each layer was recorded. Whichever layer had the highest fractional coverage of clouds was assumed to represent the visual hemispheric cloud coverage as if it had been observed from above or below; the term cloud coverage hereafter refers to this visual hemispheric cloud coverage.

Microwave emissions from the atmosphere at 23.8- and 31.4-GHz frequencies were measured using a radiometer. These emission measurements were used to compute the column-integrated water vapor (IWV) and liquid water path (LWP) through a cone of atmosphere of width 5.9° every 20 s, with uncertainties of $\sim$10 g m^{-2} for the LWP and 2% for the IWV (Revercomb et al. 2003). Upwelling and downwelling LW and SW irradiances were recorded at 1-min intervals using a surface broadband solar and infrared radiation station (SIRS) (Stoffel 2005; Augustine et al. 2000). Eppley normal incidence pyrheliometers, precision spectral pyranometers, and shaded model 8-48 ''black and white'' pyranometers are used in the SIRS for the SW measurements, and Eppley precision infrared radiometers for the LW. The spectral response for the SW detectors is limited to the 295–3000-nm interval and the 3.5–50-μm interval for the LW detectors.

A surface meteorological station continuously observed the surface temperature, relative humidity (RH), wind speed, wind direction, and rainfall rate. Measurements were made during the entirety of 2006 with the exception of the WACR, which only operated from March through December. Hourly averages of the cloud properties, LWP, IWV, and the radiative fluxes were used to produce monthly averages for comparison with GCM output.

b. GERB instrumentation and data processing

The West African Sahel is monitored by the geostationary GERB and SEVERI instruments that continuously measure the TOA radiation budget from a vantage point above 0° longitude. A north–south array of 256 blackened detectors that scans in an east–west and west–east pattern measuring the SW and total radiation constitute the GERB instrument. Total broadband spectral response for GERB is from 320 nm to >50 μm (hereafter TOT) and filters are used to subsample the SW portion of the spectrum from 320 to 4000 nm. Coincident SW and TOT images are obtained every 6 min with a 45-km nadir resolution, and "synthetic" LW radiation is computed by differencing the broadband SW and TOT radiance measurements, which provides a LW spectral range from 4000 nm to 50 μm with a maximum spectral response from 5000 nm to 50 μm. Complementing GERB is the SEVERI instrument, which measures multispectral (narrowband) images at wavelengths of 0.6, 0.8, 1.6, 3.9, 6.2, 7.3, 9.7, 10.8, 12, and 13.4 μm with spatial resolution of 3 km and a sampling period of 15 min. Filtered radiances are converted to unfiltered radiances and comparisons with coincident measurements made by the Cloud and Earth's Radiant Energy System (CERES) suggest that measured SW and TOT radiances are within 1% (Clerbaux et al. 2008a,b).

Edition 1 GERB data used in this study consist of averaged, rectified, and geolocated level 2 broadband radiance data (Harries et al. 2005). These data processing necessities add additional uncertainty to the 1% radiance measurements and the absolute accuracy of edition 1 data is estimated to vary between 2.25% and 5% for SW radiance and 1% and 2% for LW radiance (Allan et al. 2007; Dewitte et al. 2008). Gaps exist in the angular distribution of the radiance measurements made by the GERB instrument. Filling these observation gaps is accomplished using high-resolution unfiltered radiances measured by SEVERI in conjunction with an appropriate angular dependence model (ADM). These ADMs contribute additional uncertainty of order 5 W m^{-2} for LW fluxes and 10 W m^{-2} for SW fluxes (Harries et al. 2005; Loeb et al. 2001), but this uncertainty is dependent upon the number of samples that are averaged. Monthly averages of edition 1 GERB data are used in this study, which mitigates the uncertainties associated with the ADM.

Computing the cross-atmosphere radiative flux divergence requires simultaneous measurements of the SW and LW fluxes at the TOA and at the surface across the entire broadband SW and LW spectrum. Unfortunately, the AMF and GERB sensors have slightly different spectral pass bands in the SW and LW. In the SW, only 2% of solar insolation falls in the 3000–4000-nm band that is not captured by the AMF, but detected by GERB, and a negligible amount of compensation for this missing insolation is provided by the shorter minimum wavelength (295 nm for AMF as compared to 320 nm for GERB). Hence, the pass-band disparity in the SW contributes at most 2% uncertainty to calculations of the SW cross-atmosphere flux divergence using the AMF and GERB combination, which is not measurable given the uncertainty in the GERB TOA fluxes. Pass-band disparity between AMF and GERB in the LW is negligible (<1% uncertainty).

c. GCM model output

Model outputs from the GCMs used in this study were obtained from the Program for Climate Model Diagnosis and Intercomparison (PCMDI) for the Coupled Model Intercomparison Project phase 3 (CMIP3). These outputs are from simulations of the past, present, and future climate used in IPCC AR4. This collection of model results is known as the World Climate Research Program (WCRP) CMIP3 multimodel dataset (Meehl et al. 2007). Four models from the 25 available model outputs were chosen for evaluation in this study. Output from the U.K. Met Office Hadley Center for Global Environmental Modeling version 1 (HadGEM1: 1.25° latitude × 1.875° longitude, 38 layers), National Aeronautics and Space Administration Goddard Institute of Space Studies Model E-H (GISS-EH: 4° latitude × 5° longitude, 20 layers), National Oceanic and Atmospheric Administration Geophysical Fluid Dynamics Laboratory Coupled Model version 2.0 (CM2: 2.0° latitude × 2.5° longitude, 24 layers), and National Center for Atmospheric Research Community Climate System Model version 3.0 [CCSM3: 1.4° latitude × 1.4° longitude (at the equator), 26 layers] are used in this study. These models from hereon are referred to as HadGEM1, GISSEH, CM2, and CCSM3. Setups for the simulations used in AR4 are described in detail in Martin et al. (2006), Schmidt et al. (2006), Delworth et al. (2006), and Collins et al. (2006), respectively.

Simulations used in this study increase the current CO_2 concentration by 1% until the concentration doubles (~70 yr) and after that it is held constant for an additional 150 yr. Simulations made by CCSM3 were not available for this scenario, so output from the Special Report on Emission Scenarios A1B (SRES A1B) simulation in which the CO_2 concentration increases at the current rate until it reaches 720 parts per million and is assumed constant thereafter are used instead. The AR4 and CCSM3 simulations are initialized using the same conditions at the beginning of 2001, the initial year of the simulations, and the comparisons made in this study use results from 2001 to 2010. Any artifacts resulting from the use of different scenarios in AR4 and CCSM3 are likely to be minimal, but minor differences should be expected.

3. Methodology

The presence of GERB over the Sahel, accurate measurements of both surface upwelling and downwelling radiative fluxes made by the AMF, and the uniformity of the land surface in the region makes it possible to calculate the atmospheric column radiative flux divergence. This section describes the methods used to produce monthly averages of this divergence and the techniques employed to separate the radiative effects of clouds and clear sky. These techniques are applied to the AMF and GERB measurements and to the output from the AR4 models.

Upwelling and downwelling, SW and LW fluxes at the surface and TOA observed by the AMF and GERB radiometers were averaged for an hour and monthly averages of these quantities were calculated. The SW, LW, and net atmospheric column radiative divergences were calculated on monthly time scales from the AMF–GERB instrumentation and from model simulations using the equation:

$$\begin{aligned}\text{Net Rad.Div} = {} & \text{SWD}_{\text{TOA}} - \text{SWU}_{\text{TOA}} + \text{SWU}_{\text{Sfc}} \\ & - \text{SWD}_{\text{Sfc}} + \text{LWU}_{\text{Sfc}} - \text{LWD}_{\text{Sfc}} \\ & - \text{LWU}_{\text{TOA}}\end{aligned}$$

in which the terms are

Net Rad.Div	net column radiative divergence,
SWD_{TOA}	downwelling shortwave radiation at the TOA,
SWU_{TOA}	upwelling shortwave radiation at the TOA,
SWU_{Sfc}	upwelling shortwave radiation at the surface,
SWD_{Sfc}	downwelling shortwave radiation at the surface,
LWU_{Sfc}	upwelling longwave radiation at the surface,
LWD_{Sfc}	downwelling shortwave radiation at the surface,
LWU_{TOA}	upwelling longwave radiation at the TOA.

Diagnosing the impacts of clouds upon the radiation budget of the West African Sahel using AMF1 and GERB measured radiative flux divergences provides an opportunity to gain perspective on the cloud and radiation physics embodied in the AR4 GCM simulations. Traditionally, measurements of the radiative fluxes at the TOA or at the surface are used to quantify the effects of clouds at any given location and to gauge the accuracy of GCM simulations of these radiative fluxes. A standard procedure is to dissect the surface or TOA radiative fluxes into all-sky and clear-sky components and compute the cloud radiative forcing (CRF) (Ramanathan et al. 1989; Soden et al. 2004, 2008), which quantifies the effects of clouds upon the column boundary fluxes. Surface (Sfc) and TOA CRF are calculated as follows where the superscript CS refers to clear-sky, cloud-free conditions; no superscript refers to all-sky conditions; suffixes U and D refer to upwelling and downwelling; and the prefixes LW and SW maintain their definitions (all the quantities are in watts per square meter):

$$\begin{aligned}\text{Sfc CRF} = {} & \text{LWD}_{\text{Sfc}} - \text{LWD}^{\text{CS}}_{\text{Sfc}} + \text{SWD}_{\text{Sfc}} \\ & - \text{SWD}^{\text{CS}}_{\text{Sfc}},\end{aligned} \tag{1}$$

$$\begin{aligned}\text{TOA CRF} = {} & \text{LWU}^{\text{CS}}_{\text{TOA}} - \text{LWU}_{\text{TOA}} + \text{SWU}^{\text{CS}}_{\text{TOA}} \\ & - \text{SWU}_{\text{TOA}}.\end{aligned} \tag{2}$$

Calculating the clear-sky fluxes for GCM simulations entails setting the cloud fraction to zero and computing the radiative fluxes using one of the methods described in Soden et al. (2008). During these clear-sky calculations the TOA downwelling SW flux and the surface upwelling LW flux assume the all-sky values.

There are a few noteworthy limitations of the CRF technique for assessing the impact of clouds on the atmospheric radiation budget. Most importantly, measuring or computing the CRF at the surface or TOA convolves the CRF with the fluxes at the other boundary. Because the clear-sky and all-sky TOA fluxes are a function of surface albedo and surface temperature in addition to the atmospheric humidity and cloud profiles, the TOA CRF essentially quantifies the impact of clouds on the heating of the earth and atmosphere system rather than the atmosphere only. Another important consideration is that the TOA CRF depends on cloud albedo, cloud-top height, cloud coverage, surface albedo, cloud field coherence (overlap), and surface temperature. These dependencies prevent the TOA CRF at a certain location from being compared unambiguously to the TOA CRF at another location or, for that matter, to the CRF measured at a later time at the same location due differences in surface properties.

To ameliorate some of the limitations imposed by the CRF it is possible to use the cross-atmosphere radiative flux divergence to investigate the integrated effects of cloudiness upon the column itself. Atmospheric column radiative flux divergence for all-sky conditions described in (1) can be calculated for clear-sky conditions using

$$\begin{aligned}\text{CS Net Rad.Div} = {} & \text{SWD}^{\text{CS}}_{\text{TOA}} - \text{SWU}^{\text{CS}}_{\text{TOA}} + \text{SWU}^{\text{CS}}_{\text{Sfc}} \\ & - \text{SWD}^{\text{CS}}_{\text{Sfc}} + \text{LWU}^{\text{CS}}_{\text{Sfc}} - \text{LWD}^{\text{CS}}_{\text{Sfc}} \\ & - \text{LWU}^{\text{CS}}_{\text{TOA}}.\end{aligned} \tag{3}$$

This column radiative divergence accounts for the radiative fluxes at both boundaries, so the difference between the all-sky radiative divergence and clear-sky radiative divergence only depends on the cloud properties and not the surface properties. Cloud radiative effect (CRE) is defined as the difference between the all-sky atmospheric column radiative divergence and the clear-sky atmospheric radiative divergence and is given by

$$\mathrm{CRE} = \mathrm{Net\ Div} - \mathrm{Net\ Div}_{\mathrm{CS}}. \tag{4}$$

It only depends on the cloud properties in the column (cloud fraction, cloud-top temperature, etc.) and its relationship with the CRF is written as

$$\mathrm{CRE} = \mathrm{TOA\ CRF} - \mathrm{Sfc.CRF} + \mathrm{SWU}_{\mathrm{Sfc}} - \mathrm{SWU}_{\mathrm{Sfc}}^{\mathrm{CS}}. \tag{5}$$

Clouds impact the atmospheric radiation budget in the Sahel region of West Africa according to these relationships, so a comparison between measured and GCM-simulated values of the CRE contains fundamental information about the interworkings of the radiation transfer in the Sahelian atmosphere and the integrity of GCM simulations of its mechanics.

Past efforts to measure the cross-atmosphere cloudy-sky absorption have often relied on short duration snapshots of the TOA radiation fluxes from polar-orbiting satellites, which are demonstrably inconsistent with the time scale of many cloud-induced changes in the radiation budget and, thereby, fail to attenuate the impacts of cloud field randomness. Successful measurement of the CRE and the associated surface and TOA CRF using the GERB and AMF data employing the procedure described in the appendix enables a comparison of the CRF and CRE measurement techniques and a diagnosis of the cloudy-sky absorption in the Sahaelian atmosphere.

4. Results

Climate models are not designed to accurately produce the atmospheric structure for a given year, though it may be asserted that they should be able to capture the range of conditions that are observed over a period of a decade or so. A decadal envelope formed by the maximum and minimum values of the monthly averages simulated by the GCMs may include multiple El Niño and La Niña cycles along with other periodicities of climatic import. Measurements collected during a single year, in this case 2006, are expected to be members of the set bounded by the extreme values of the monthly averages for a given GCM during the decade centered on 2006 (from 2001 to 2010), which is hereafter termed the decadal envelope. Many types of measurements collected during 2006 using the AMF1 and GERB sensors are compared with their GCM counterparts in the sections that follow under the basic assumption that model skill is indicated qualitatively by the inclusion of the measured values within the decadal envelope of GCM monthly average extremes. Results presented forthwith are not sensitive to the choice of a decade as the time period of merit, and virtually the same results are obtained when the GCM solution envelope is stretched to 30 years. Attempts are made in the latter half of this section to explore the CRE in the Sahel region using AMF1 and GERB measurements and to investigate the representation of the CRE in two of the four GCMs.

Annual wet season precipitation is critical to life in the Sahel, whereupon the wet season precipitation flux is a seminal GCM forecast variable for this region. Precipitation flux also influences the cross-atmosphere radiative flux divergence and CRE through its ability to redistribute and remove water from the atmospheric column. Shown in Fig. 2 are the decadal envelopes of the precipitation fluxes produced by the four GCMs. Miniscule precipitation was observed during the dry season (October–May) in all four GCMs with almost all precipitation observed during the wet season (June–September). Observations suggest the onset of monsoon to be subtle—with the precipitation flux increasing from 0.5 kg m^{-2} day^{-1} in June to 5 kg m^{-2} day^{-1} in July and then decreasing gradually to zero by October. The shape of the wet season precipitation flux curve and its magnitude during 2006 agree well with results from a recent study of the precipitation flux that spans a 30-yr period (Lélé and Lamb 2010).

While all four GCMs simulated the basic structure of the observed annual cycle of the precipitation flux, they exhibited a wide range of skill with respect to the timing and magnitude of wet season precipitation, which is consistent with the findings in past GCM studies in other semiarid regions (Ruiz-Barradas and Nigam 2006). As an example of the type of month-to-month variability observed in the GCM simulations in a single year, results from the individual year 2006 are plotted within the decadal envelope; aside from adding perspective on typical seasonal variability, they should not be compared directly to the magnitudes of the AMF1 measurements. All four GCMs simulated dry seasons that are shorter than the observed eight months and wet seasons that were longer than observed. Encroachment of the simulated wet season into the dry season was most apparent in CCSM3 and CM2, which produced large precipitation fluxes during the observed dry season. Though the monsoon season was slightly elongated in GISS-EH and HadGEM1, their simulated precipitation fluxes compared well with observations. Conversely, in addition to lengthening the wet season, the precipitation fluxes predicted by CCSM3

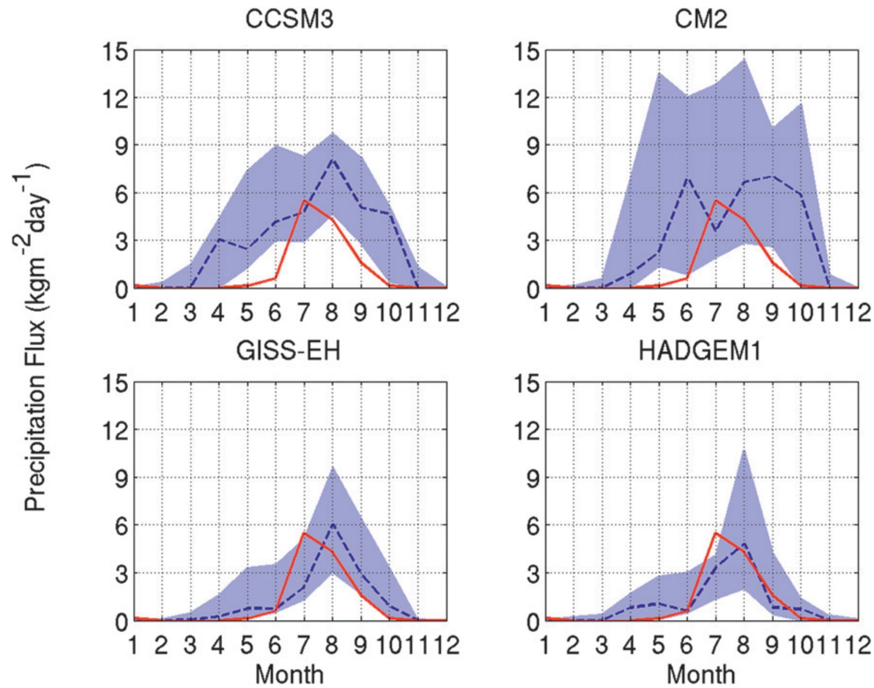

FIG. 2. Envelope of maximum and minimum monthly averaged precipitation flux as simulated by the four GCMs (light blue shading) for the period from 2001 to 2010, the GCM-simulated value for 2006 (blue dashed line), and observations from the AMF1 (red) for months during the year 2006.

and CM2 were significantly overestimated. The GISS-EH GCM exhibited the smallest decadal range of monthly averaged precipitation fluxes, while CM2 exhibited the largest. Simulated year 2006 fluxes in the various GCMs demonstrate that CCSM3 and CM2 tend to produce highly variable month-to-month averages that act to widen the decadal envelope. Detailed time series analysis of precipitation flux for the decade centered on the year 2006 (not shown) shows that CM2 produces a two-yr-long spike in the precipitation flux, which was mostly responsible for its large simulated range of precipitation flux during the decade: no other GCM produced a similar spike.

Choosing extremes in the monthly averages to gauge GCM performance as in Fig. 2 ignores any month-to-month coherence in the precipitation flux signal in the four GCMs that may be caused by large-scale seasonal patterns. An alternative approach is to define the performance envelope as being bounded by the years with the maximum and minimum yearly total precipitation. These years do not, for the most part, match the monthly average maximum–minimum bounds plotted in Fig. 2 and it can be concluded that uncorrelated monthly fluctuations in these GCMs appear more relevant to the structure of the precipitation flux in this region than any sort of month-to-month coherence driven by some longer time-scale forcing. This does not mean that the yearly signals are not important, just not dominant in the GCM simulations of precipitation.

Monthly average IWV measured using the AMF1 microwave radiometer in 2006 is compared with the decadal range of simulated IWV values produced by CCSM3, CM2, and GISS-EH for the 2001–10 envelope (Fig. 3). Monthly averaged IWV values were not available for the HadGEM1 simulations. All three GCMs capture the annual cycle in IWV but have a general tendency to underestimate IWV during January and February relative to observations. Simulated IWV for the entire year is minimum for CCSM3 and maximum for GISS-EH. Unlike the comparisons with precipitation flux that show widely differing views of monthly variability, these comparisons show that all three GCMs exhibit relatively similar monthly variability as indicated by the similar widths of their decadal envelopes.

Monthly averaged total water path and ice water path reported by each of the four GCMs for 2001–10 were used to compute the liquid water path (LWP), which is compared to the AMF measurements in Fig. 4. Overall, CCSM3 and CM2 are able to capture the annual cycle of LWP, though the models differ substantially in their portrayal of decadal monthly variability. The CM2 GCM simulated a wide range in the LWP during the decade of 2000–10 with the monthly averaged LWP ranging from

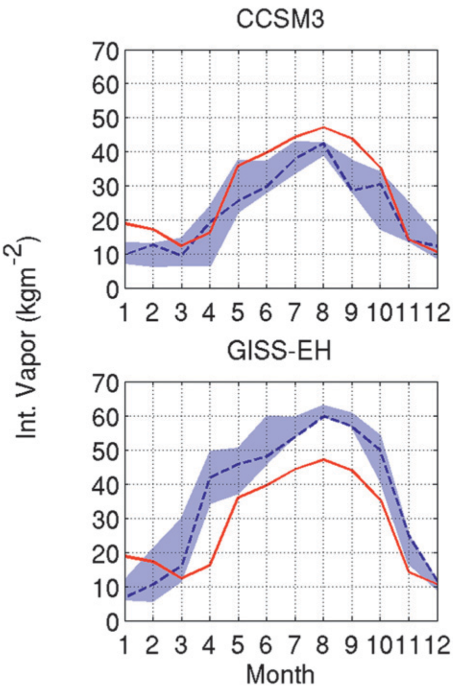

FIG. 3. As in Fig. 2 but for column-integrated water vapor. The integrated water vapor (IWV) was not available from the Hadley model on the CMIP3 web site.

almost 0 to 0.18 kg m^{-2} during the month of July. During 2006 the CM2 LWP was unusually high during January–April but decreased to 0.025 kg m^{-2} at the beginning of the wet season and remained relatively constant thereafter. Variability during this single year lies in stark contrast to the width of the decadal envelope, which is a reflection of large year-to-year variability simulated during the decade. It is shown later that the CM2 model was producing substantial cloudiness during the wet season despite its negligible LWP, which suggests that the clouds

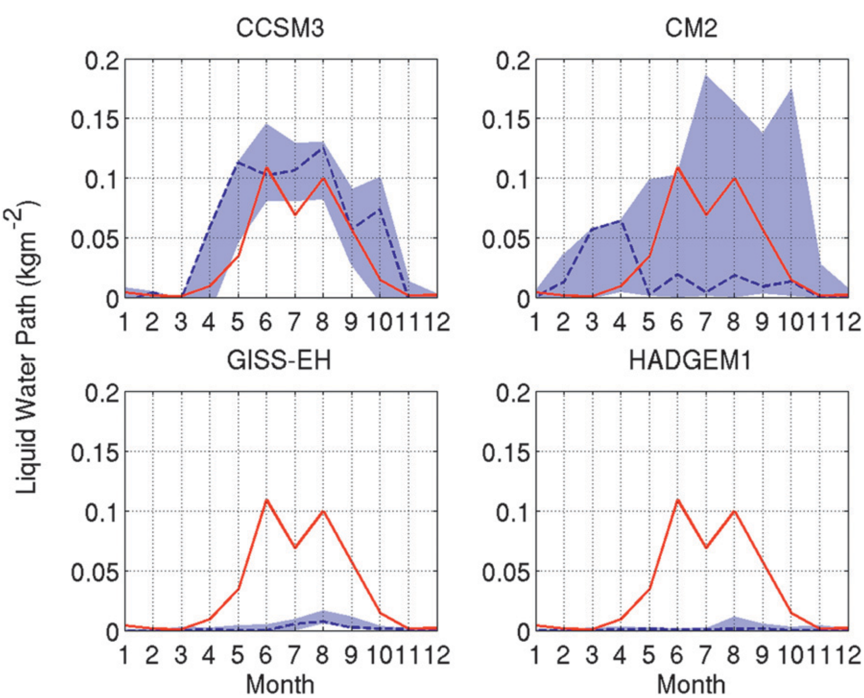

FIG. 4. As in Fig. 3 but for column-integrated liquid water path (LWP).

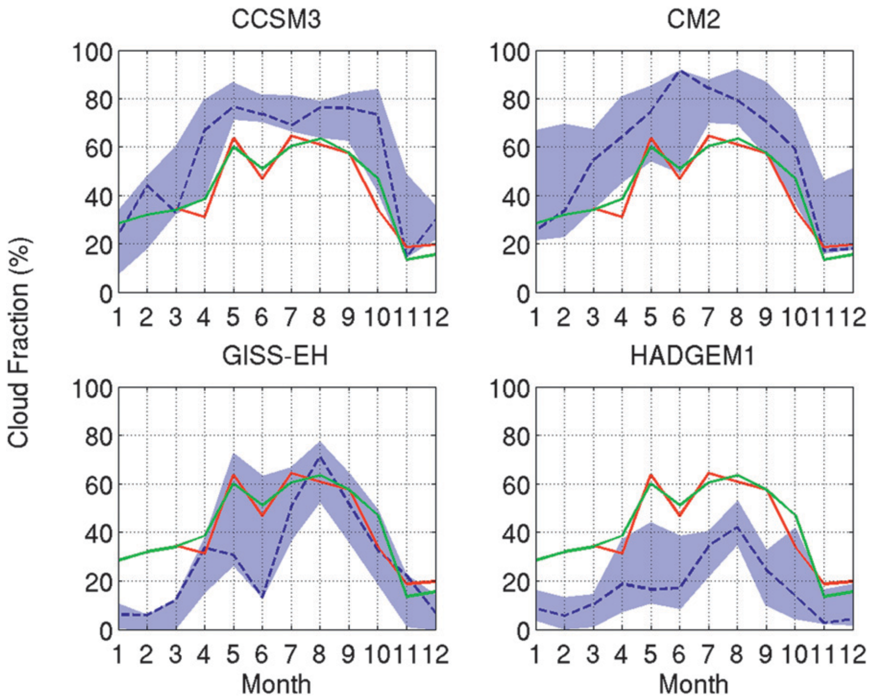

FIG. 5. As in Fig. 4 but for the areal cloud fraction. The ISCCP observed areal cloud fractions are also plotted (green).

simulated by the CM2 during the wet season in 2006 are mainly high-level ice clouds. Both GISS-EH and HadGEM1 simulated a narrow range of LWP in 2006 that is significantly lower than that observed by the AMF microwave radiometer but also produce substantial cloudiness, leading to the supposition that the clouds must be composed mostly of ice.

Monthly averaged cloud coverage derived from AMF observations in 2006 are compared with the decadal envelope of cloud coverage produced by each of the four GCMs in Fig. 5. Cloud observations were not available from the AMF for January and February of 2006 owing to a delayed deployment of the WACR. Also shown is the monthly cloud coverage as reported by the International Satellite Cloud Climatology (ISCCP) visible+IR algorithm as reported by the ISCCP D2 level dataset (Rossow and Schiffer 1991; Rossow and Dueñas 2004). Excellent agreement is noted between the AMF observed cloud coverage and the ISCCP reported cloud coverage; for example, both platforms record a similar "dip" in the cloud coverage during the month of June. Cloud coverage during the dry season varies from 20% to 40% and increases to 60% during the wet season and all four GCMs exhibit an annual cycle in cloudiness. The GISS-EH-simulated cloud coverage for the months of January–March and December was about 5%, which corresponds to only one-quarter of the observed cloud coverage, while its simulated cloud coverage from April to November agrees well with the observations. Simulated cloud coverage in HadGEM1 is lower than the observed amount during the entire year and produces only 40% of the observed during its wet season. A general overestimation of the cloud coverage is seen in the output from CCSM3 and CM2 and the latter produces a June 2006 that is the cloudiest of the decade; coincidently, these two GCMs also overestimate the precipitation flux. Ironically, GISS-EH indicates that June 2006 is the least cloudy June of the decade, while August 2006 is nearly the cloudiest August of the decade, therein implying that there is wide month-to-month variability in cloud coverage during the wet season in this GCM. In general, GISS-EH is the sole GCM of the four that simulated cloud coverage within the bounds of the decadal envelope and is also one of two GCMs that also correctly simulated the precipitation flux.

Attention is now turned to the cross-atmosphere radiation budget after documenting many of its primary controls above: the LW, SW, and net radiative flux divergence measurements for the year of 2006 are compared with the GCM-simulated values in Fig. 6. The surface downwelling LW radiative flux from GISS-EH was not available, so the LW and net radiative flux divergences could not be calculated. The measured SW radiative divergence was positive throughout the year,

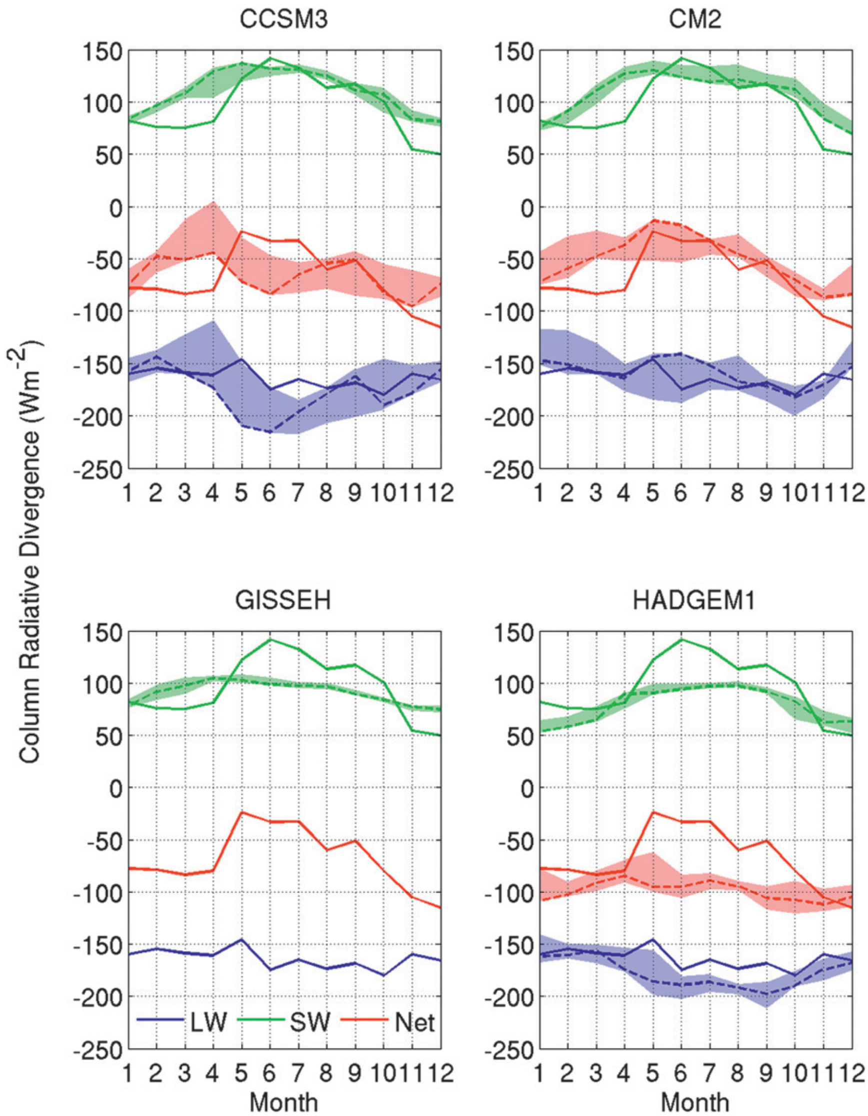

FIG. 6. Envelope of maximum and minimum monthly averaged SW (green), LW (blue), and total (red) column-integrated radiative divergence as simulated by the four GCMs (shading) for the period from 2001 to 2010, the GCM-simulated value for 2006 (dashed lines), and observations from the AMF1 (solid lines) for months in year 2006.

denoting heating of the atmosphere by SW radiation, and it peaked at 145 W m^{-2} in June at the beginning of the wet season. Annual mean SW radiative divergence was 107 W m^{-2}. Meanwhile, the measured LW radiative flux divergence was negative throughout the year, denoting cooling of the atmosphere, and its minimum was -180 W m^{-2}. The annual mean LW radiative divergence was -164 W m^{-2} and the net column radiative flux divergence was also negative throughout the year; its annual mean is -52 W m^{-2}. Correlation coefficients of cloud coverage with SW, LW, and net radiative flux divergences are 0.85, -0.05, and 0.75, respectively—indicative of the first-order impact that clouds exert upon the SW radiative absorption.

All of the GCMs for which LW data were available (three out of the four studied) simulate the LW divergence in the Sahel with reasonable accuracy, while all four GCMs show somewhat less skill in simulating the SW divergence. This reduction in skill contributes to a misrepresentation of the net radiative flux divergence that is particularly acute in HadGEM1 during the wet season and in CCSM3 and CM2 during the dry season. Individually, the CCSM3-simulated net radiative flux divergence disagrees considerably with the observations during the dry season and wet season transition and it simulates a lower than observed LW divergence during the wet season. Apart from considerable discrepancies in the dry season in the CM2 GCM that are found in the SW and net divergences, its simulated net radiative divergence matches remarkably well with the observed net divergence in the wet season. In contrast, the HadGEM1 simulated net radiative divergence is much lower than the observed values during the wet season, primarily as a consequence of its estimate of the SW divergence.

Having established the net measured LW, SW, and net radiative flux divergences over the region, the role of clouds in modulating these divergences and the utility of the CRE as a new GCM analysis tool is investigated. The basic idea is to dissect the measured cross-atmosphere radiative flux divergences into clear-sky and all-sky components and compute the difference, which is the CRE. Performing a similar decomposition in GCMs enables a comparison between measured and simulated CREs and, therein, a more detailed assessment of the integrity with which the GCMs represent cloud–radiation interactions. Ancillary to this objective is the associated goal of measuring the relationship between the surface and TOA CRFs, which characterize the radiative impacts of clouds at the boundaries of the column, and the CRE, which characterizes the radiative impacts upon the column itself, and therefore, hopefully, reconciling the relationships between these three radiative components. Techniques used to measure the surface and TOA CRF, which are ultimately used to measure the CRE, are discussed in the appendix. Not all of the radiative fluxes needed to calculate the CRF and CRE are available for CCSM3 and GISS-EH but they are available for CM2 and HadGEM1, and an analysis of the CREs in these two models against measurements is described forthwith.

Computing the CRF for CM2 and HadGEM1 is straightforward because the clear-sky LW and SW fluxes at the surface and TOA are determined in the radiation codes and provided in the model output. Monthly averaged values of the SW, LW, and net CRF at the surface and TOA from CM2 and HadGEM1 are plotted along with the observed values for the year 2006 in Figs. 7 and 8. The SW TOA CRF and SW Sfc CRF are negative in both GCMs, indicating a cooling effect of clouds on the earth+atmosphere system (TOA CRF) and on the earth's surface (surface CRF). This is mainly due to the clouds being more reflective than the underlying land surface (higher albedo). Comparison of the width of the decadal maximum–minimum envelope in the two GCMs reveals that CM2 is considerably more variable in its depiction of SW CRF. Both GCMs produce reasonable estimates of the SW TOA CRF and both produce unrealistically small estimates of the SW surface CRF. Wet season SW surface CRF estimates differ from the measurements by over 100 W m^{-2} in HadGEM1, indicating that the surface cooling due to cloud cover in this GCM is grossly underestimated. Such an underestimate is bound to impact the convective triggering in this model, which is stability dependent. Viewing these results within the context of Fig. 5 suggests that the underestimate of cloud coverage in HadGEM1 may be a contributing factor to its underestimate of SW surface CRF. An overestimate in the cloud coverage in CM2 combined with a slight underestimate of surface CRF suggests a problem with the SW radiative properties of the clouds themselves.

Measured LW TOA and surface CRF are significantly positive, indicating that the clouds heat the earth+atmosphere system and the earth's surface. Representation of the LW TOA is excellent in CM2, while HadGEM1 produces considerably less heating in cloudy conditions than the observations suggest. Both GCMs produce zero LW heating at the surface in response to clouds, in stark contrast to the measurements that show that the clouds produce considerable LW heating at the surface. Routine surface observations taken at night and taken at almost any geographic location show that cloud cover is almost always associated with warmer than average nighttime low temperatures; these impacts are notably missing from the two GCMs. In these models, radiative cooling at night will occur at the same rate regardless of cloud cover, which seems physically unrealistic.

Summing SW and LW surface measured CRF produces a negative net surface CRF throughout the year indicating that clouds have a cooling effect on the surface regardless of the season. At the TOA the net CRF exhibits minor warming ($\sim$20 W m^{-2}) until April, after which it increases to $\sim$40 W m^{-2} in May and gradually decreases through the wet season. While CM2 represents the net TOA and surface CRF extremely well, its excellent performance at the surface is due to the canceling of significant errors in the LW and SW CRF. It is evident from Figs. 8e,f that HadGEM1 produces nearly zero net CRF through most of the year and only a modest surface net CRF during the wet season. Clouds would appear to have an extremely minor impact on the column radiative heating in this region in the HadGEM1 GCM. Both GCMs seem to more accurately estimate the TOA LW, SW, and net CRF. This is likely due to a heavy reliance on satellite data to constrain radiative transfer at the TOA and the use of these data to determine global cloud radiative properties.

Computing the CRE for the CM2 and HadGEM1, which determines the net heating or cooling in the

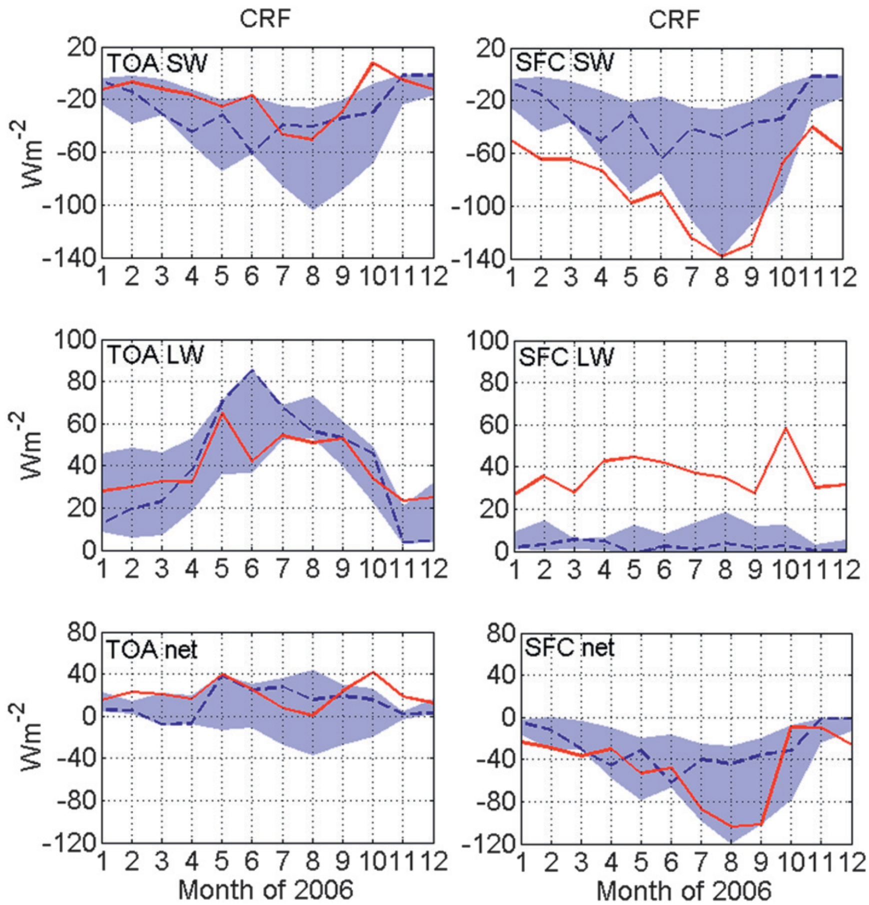

FIG. 7. Envelope of maximum and minimum monthly averaged TOAs and surface cloud radiative forcing (CRF) as simulated by CM2 (blue shading) for the period from 2001 to 2010, the GCM-simulated value for 2006 (dashed blue lines), and observations from the AMF1 (red lines) for months in year 2006.

atmospheric column itself as a result of cloud cover, is straightforward given the clear-sky divergence. This clear-sky divergence is shown in Fig. 9 alongside the AMF1–GERB measurements. These clear-sky divergences, in general, show larger discrepancies between the simulated and measured values than the all-sky divergences shown in Fig. 6, which are reproduced in the lower panel for comparison. Exaggerated SW heating is observed throughout the year in CM2 and in HadGEM1 with the exaggeration in CM2 being particularly large. Error cancelation in both GCMs produces a net clear-sky divergence that agrees better with the measured values than either of its constituents (SW and LW clear-sky divergences). Absorption due to water vapor, and to a lesser extent dust, in CM2 and HadGEM1 must be responsible for the observed differences between the simulated and measured SW and LW divergences.

These foundation calculations culminate in the plots of the SW, LW, and net CRE shown in Fig. 10. Glaring discrepancies are evident in the SW CRE in both GCMs, which in essence predict no radiative warming in the column when clouds are present, while measurements show that this warming can exceed 70 W m^{-2} during September. Measurements show that there is a near-zero LW CRE, which is well captured by HadGEM1. Ironically, the enhanced LW CRE exhibited by CM2 somewhat approximates its diminished SW CRE, leading to a net CRE that agrees fairly well with the measurements. Despite success in reproducing the measured LW CRE in HadGEM1, its underestimate of SW CRE dominates the net CRE, so HadGEM1 seriously underestimates the radiative heating impacts of clouds in the region.

5. Summary and discussion

An unprecedented opportunity to simultaneously observe the annual cycles of precipitation, IWV, LWP, cloud

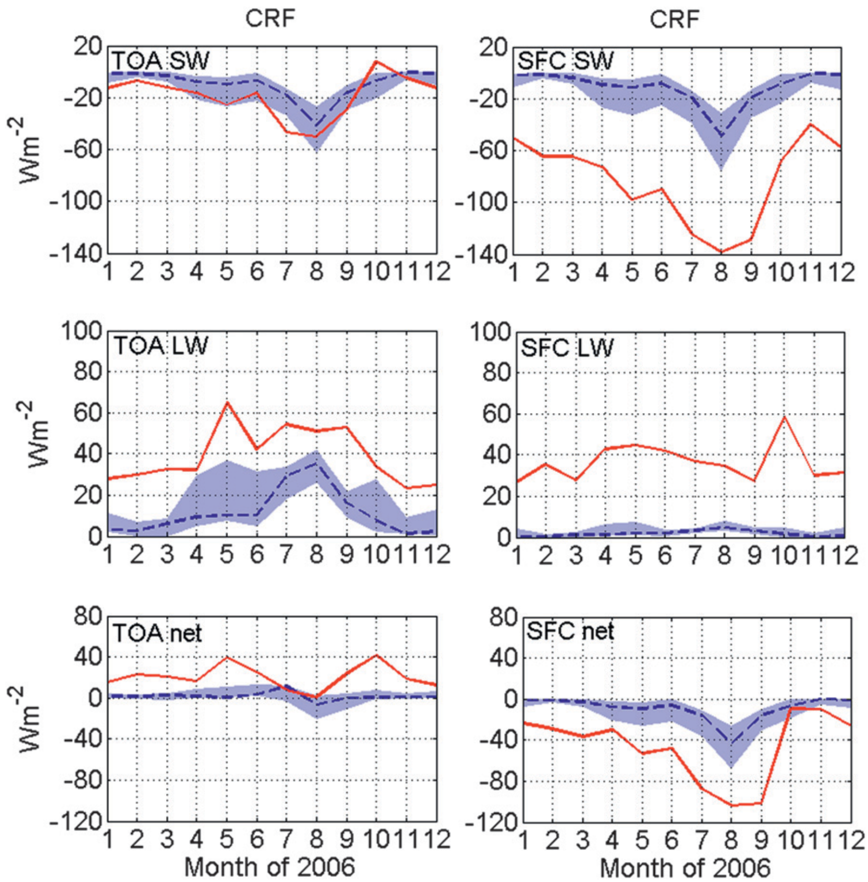

FIG. 8. As in Fig. 7 but for HadGEM1.

areal coverage, and the corresponding cross-atmosphere radiative flux divergence was realized as a consequence of the AMF1 deployment at Niamey, Niger, in 2006 and the colocation of the GERB instrument above this region. Detailed measurements of the SW, LW, and net radiation divergence, along with measurements of the CRF and CRE were made. This suite of measurements enabled the column-integrated cloud and radiation interactions in this region to be characterized in intracate detail. These data were used to evaluate the simulations of the annual cycles of precipitation, IWV, LWP, cloud areal coverage, and cross-atmosphere radiation budget in the Sahel region as depicted in four GCMs that were used in the IPCC AR4. A particular focus was placed on the detailed role of clouds and clear sky in modulating the cross-atmosphere radiative flux divergence in two GCMs that provided the necessary output to facilitate the analysis: CM2 and HadGEM1.

Precipitation flux magnitude and wet-season signal shape were deemed superior in GISS-EH and HadGEM1, but they display inconsistencies in their depiction of cloud microphysics despite their relatively accurate depictions of precipitation. For example, GISS-EH produces clouds that are predominantly composed of ice water, which is why so little liquid water is indicated in Fig. 4. Ironically, HadGEM1 produces too few clouds and a miniscule amount of total water, which is to say that there is neither liquid nor ice in the clouds, yet the clouds produce a reasonable amount of precipitation. It is also evident that accurate simulation of precipitation seems disconnected from the accurate simulation of cross-atmosphere radiative flux divergence in this region: in at least one case, CM2, the convective precipitation efficiency is adjusted until net radiative closure is achieved.

There are two thematic approaches, bulk and ensemble, used to parameterize convection and, ultimately, convective precipitation in GCMs, and the choice between them significantly impacts the precipitation flux. All GCMs use a mass-flux approach to simulate convective clouds, and stability is often used as the variable that determines the convective mass flux at cloud base. A bulk parameterization operates on the diagnosed mass flux using a representation of convective clouds that is often limited to one or two updrafts and companion

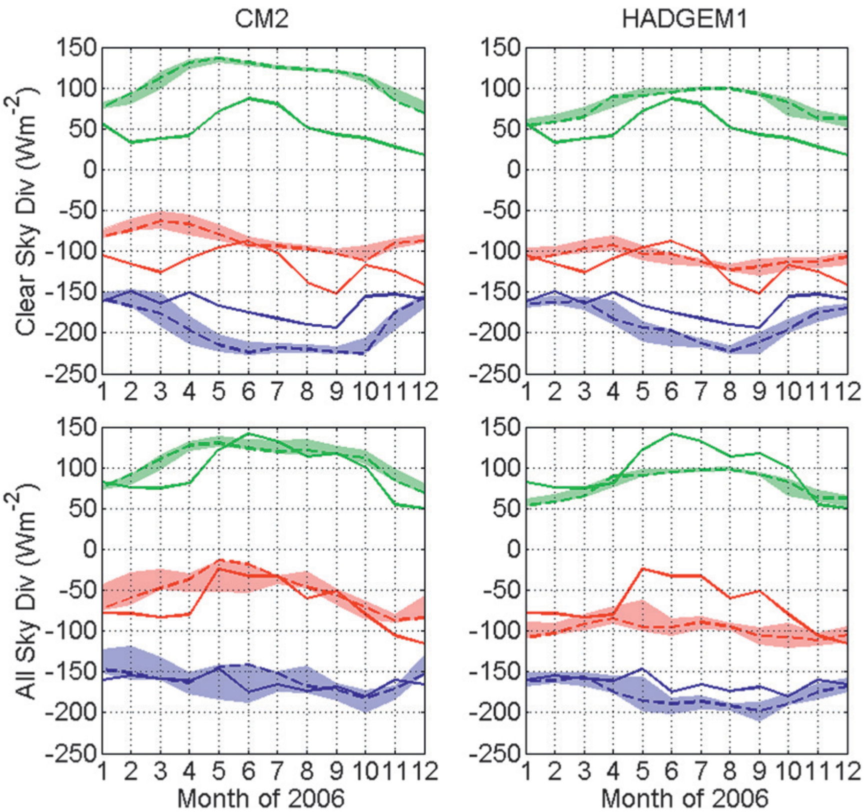

FIG. 9. Envelope of maximum and minimum monthly averaged SW (green), LW (blue), and total (red) column-integrated radiative divergence for (top) clear sky and (bottom) all sky in (left) CM2 and (right) HadGEM1 during the period from 2001 to 2010 (shaded areas), the GCM-simulated value for 2006 (dashed lines), and observations from the AMF1 (solid lines) for months in year 2006.

downdrafts meant to characterize the cloud field as a whole. Bulk approaches allow for microphysically based representations of convective precipitation, and bulk schemes are used in HadGEM1 and GISS-EH, though the latter uses a slightly modified version. Ensemble approaches to convective parameterization prescribe a spectrum of convective elements (one for each vertical layer) based upon the diagnosed mass fluxes. Ensemble parameterizations typically trade off detailed cloud microphysics for more detailed descriptions of cloud-field exchanges with the large scale environment. Convective precipitation in these ensemble schemes typically relies upon a precipitation efficiency coefficient or autoconversion rate to convert cloud water to precipitation in the absence of detailed cloud microphysics. Results presented in Fig. 2 suggest a clear separation in model skill at predicting precipitation fluxes over the Sahel between models that use a bulk approach (GISS-EH and HadGEM1) and models that use an ensemble approach (CCSM3 and CM2)—the bulk approach is superior in this region during 2006.

Moisture supply in the region during 2006 was investigated using monthly averaged AMF1-observed IWV, and in this aspect the models produced excellent results. Of the four GCMs, CCSM3 provided the best estimate of cloud LWP, though it significantly overestimated precipitation, while CM2 produced suspiciously large variability in LWP and GISS-EH and HadGEM1 grossly underestimated LWP. Shortcomings of this nature are strongly suggestive of issues related to the development of low-level convective clouds in the models, which, like rainfall, is likely a consequence of the convective parameterization. Ironically, the two GCMs that best represented the wet season rainfall produced the poorest representations of the cloud coverage and microphysical structure, with HadGEM1 producing miniscule IWP and negligible total cloud water while GISS-EH produced almost all ice during the wet season. Production and partitioning of cloud water and ice and the generation of precipitation from clouds seem problematic in all four GCMs considered in this study. Insofar as these characteristics are intricately related to radiation

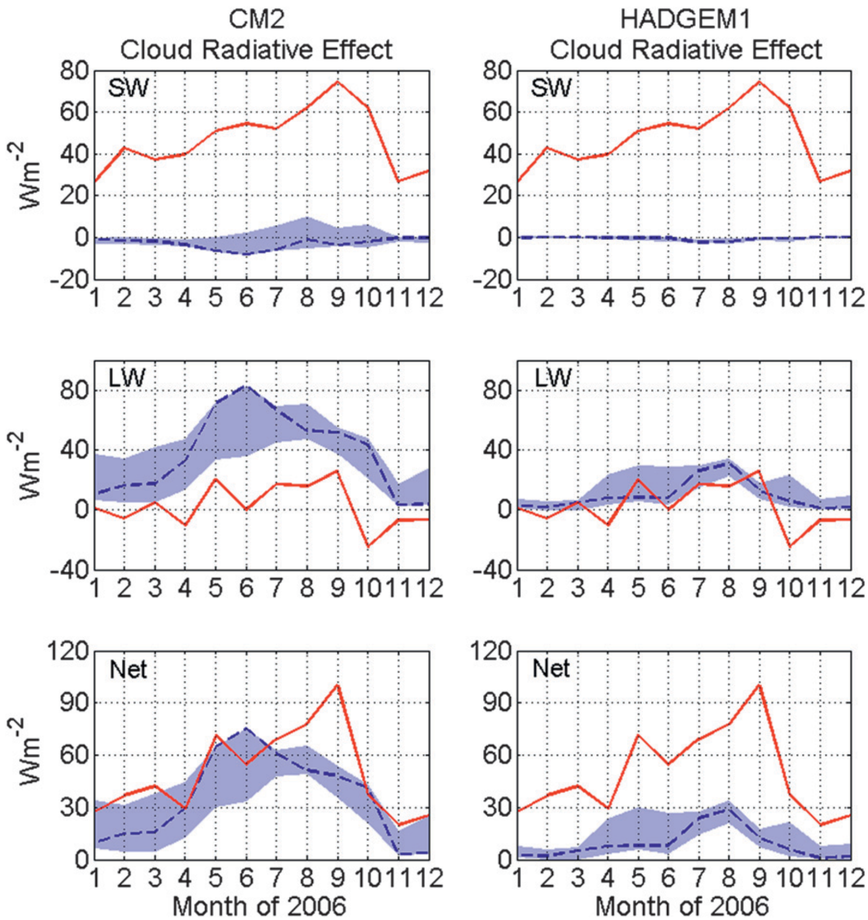

FIG. 10. Envelope of maximum and minimum monthly averaged cloud radiative effect (CRE) in (left) CM2 and (right) HadGEM1 during the period from 2001 to 2010 (shaded blue areas), the GCM-simulated value for 2006 (dashed blue lines), and observations from the AMF1 (solid red lines) for months in year 2006.

throughput in West Africa, it seems that this is a potentially severe problem.

Two categories of GCM performance with respect to radiative flux divergence emerge: CCSM3 and CM2 perform admirably during the wet season and GISS-EH and HadGEM1 perform acceptably during the dry season. Tuning properties in these GCMs include both cloud properties and precipitation, leaving it to the discretion of the GCM creators to prioritize between correct radiation and correct precipitation—a difficult decision. Net radiative cross-atmosphere flux divergence mocks the performance of the SW flux divergence, and CCSM3 and CM2 underestimate the net radiative cooling during the dry season as a result. This underestimation may be associated with the exaggeration of wet season duration in these GCMs, given that there are surely dynamic links invoked as a consequence of this underestimate. Given a cursory glance, LW flux divergence appears to be well characterized, but deeper investigation suggests that this is a façade created by error cancelation in clear and cloudy conditions in two GCMs for which a deeper analysis was feasible.

Output from two GCMs, CM2 and HadGEM1, enabled a diagnosis of the relative role of clear and cloudy skies in the SW, LW, and net CRF and CRE. Dissecting the measured cross-atmosphere radiative flux divergence into its clear-sky and all-sky components produced measured yearly averages of the SW TOA CRF, surface CRF, and CRE of ~ -19, -83, and 47 W m^{-2}, respectively, and yearly averages of the LW TOA CRF, surface CRF, and CRE of $\sim$39, 37, and 2 W m^{-2}. Notably, the SW CRE is sensitive to the estimate of clear-sky fluxes and, as explained in the appendix, the conservative technique used in these calculations may be prone to slight underestimates in the CRE at midrange zenith angles. First, addressing the impacts of clouds on the surface and TOA, the CM2 TOA, LW, SW, and net CRFs were in general agreement with the measurements, while HadGEM1 suffered difficulties with the TOA LW CRF that adversely impacted its representation of the net CRF. Both GCMs struggled to accurately characterize the surface CRF; they underestimated the SW CRF and produced approximately a zero surface LW CRF. This latter comparison is particularly disturbing because the measured surface LW CRF is significant ($\sim$30 W m^{-2}). Intuitively and quantitatively this is an important omission; when humid and cloudy conditions are present, these two GCMs treat LW radiation as if it were dry and clear. There is no doubt that this problem will adversely impact the diurnal cycle in the GCMs in this region, and it is likely to have far-reaching consequences in other parts of the model. Looking exclusively at the net surface CRF leads to the conclusion that CM2 is quite accurate in its assessment, but measurements show that this agreement is due to error cancelation: underestimate of surface SW cooling in cloudy conditions and no LW heating when measurements show that significant heating is present.

Reproducing the contrasting radiation impacts on the column itself for clear and cloudy conditions as measured by the CRE in CM2 and HadGEM1 exposed problems, which is not surprising since the TOA and surface CRFs are contributors to the CRE. Clear-sky SW radiative heating is overstated in both CM2 and HadGEM1, but particularly so in CM2. Comparatively, clear-sky LW cooling is also overestimated at approximately the same magnitude as the underestimated SW radiative heating. This combination therein produces a reasonable estimate of the net clear-sky divergence in HadGEM1 and significantly exaggerated net radiative cooling in CM2. When clouds are present, both GCMs produce a near-zero SW CRE, while measurements show that the actual SW CRE ranges from $\sim$25 W m^{-2} during the dry season to $\sim$70 W m^{-2} during the wet season. A near-zero measured LW CRE is somewhat faithfully reproduced in HadGEM1, but LW heating during cloudy conditions in CM2 is inflated. Errors in the SW and LW CREs cancel in CM2, producing a reasonable estimate of the net CRE, but do not cancel in HadGEM1, producing a vastly lower CRE than observed. In essence, HadGEM1 is penalized for correctly simulating the LW CRE because its SW CRE is near zero.

A synthesis of the impact of cloudiness on the cross-atmosphere radiative flux divergence in this region begins with the sound performance of HadGEM1 in simulating the net clear-sky radiative flux divergence, though it does so because errors in the LW and SW components cancel. This same structural combination of canceling errors is found in CM2, though its net flux suffers a bit more because of more serious difficulties in simulating the clear-sky SW flux divergence. Radiative impacts of cloud cover on the SW and LW radiation at the surface are not well simulated in CM2, but errors again cancel to produce reasonable net surface radiation. Cloud impacts at the surface in both the LW and SW are negligible in HadGEM1, which is a serious problem. Heavy reliance upon satellite estimates of the radiation budget to adjust GCMs is circumstantially evident in CM2, but less obvious in HadGEM1 based on this study. Summarizing this analysis, neither GCM accurately simulates all three components (LW, SW, and net) of the cloud radiation effect (CRE).

Measurements of CRE are available from research in the tropical western Pacific (TWP) region (Manus Island) where the IWV is 5.4 cm (McFarlane et al. 2008, their Table 2), comparable to the $\sim$4.5 cm during the wet season in the present study. Findings in this related study suggest that clouds at Manus Island exert a minimal impact upon integrated SW absorption and act primarily to redistribute heat within the column. Experiments in that study using synthetically reduced IWVs representative of the southern Great Plains ($\sim$2.5 cm) demonstrated a significantly greater CRE, thereby establishing a firm link between IWV and CRE when tropical cloud structure is present. Results from the current study reinforce the results of McFarlane et al.; a considerably larger CRE is present in the Sahel than in the TWP, particularly during the wet season. In contrast, the agreement between the measurements in McFarlane et al. and calculations performed using a radiation transfer model are generally better than the comparisons between the measured and GCM-simulated CRE in the present study. Unlike the McFarlane et al. (2008) study, observed biases in the CRE in the present study are sensitive to measurement and GCM discrepancies in the clear-sky SW divergence, which are likely due to the improper specification of the aerosol radiative properties in the GCMs: recently published evidence supports this claim (Freidenreich and Ramaswamy 2011).

Measurements of the SW, LW, and net cross-atmosphere radiative flux divergence compared with the GCM simulations reveal that, in general, the SW cross-atmosphere flux divergence is the most challenging to accurately simulate and to measure. This discovery is not shocking given the complexity of the interaction of clouds, water vapor, and aerosol with the SW radiation stream. Underestimates of the simulated SW absorption in cloudy conditions relative to observations is not a new problem in the radiation community and a recent study has implicated sampling issues between the surface and satellite observations as a contributing factor (Parding et al. 2011). The present study may suffer from similar sampling issues, but the observed discrepancy in the clear-sky SW cross-atmosphere flux divergence in two GCMs relative to measurements suggests that other issues are also contributing. Insofar as the differences between the measured and GCM-simulated SW cross-atmosphere flux divergence remain only loosely and circumstantially explained in the present study, and in many past studies, it is advisable that the radiation community continue to explore this issue.

Deciphering the relationship between the cross-atmosphere radiative flux divergence and its controls in these GCMs is exceedingly difficult due to the sparsity of information available in the GCM output. Comprehensive evaluation requires that details of the simulated cloudiness be available in the GCM output and that future observations include variables that the GCM imports into its radiation code. Conspicuously absent is a separation of all cloud variables into convective and stratiform components. Such a separation is essential to diagnosing which parameterization was invoked to produce the precipitation and to enable GCM and measurement comparisons.

Continuous measurements of the cross-atmosphere radiative flux divergence in coincidence with detailed measurements of cloud structure that were made in 2006 in West Africa enable direct measurement of the surface CRF, TOA CRF, and CRE. This measurement approach is a valuable evaluation tool for GCMs and a powerful analysis tool for studies of cloud–radiation interactions within the climate system. Measurements of cross-atmosphere radiative flux divergence and the radiatively active components within the column are currently available at specific places and times from polar-orbiting satellites. More detailed characterizations of the regional impacts of clouds will be possible if appropriately instrumented and strategically located surface sites were to be monitored by geostationary satellites making continuous, detailed measurements of the TOA radiative fluxes. Information gleaned from these sites could be extrapolated to a global scale using current and future generations of polar-orbiting satellites. In parallel, a focused effort by the GCM community to output detailed information from the simulations at these sites would be necessary to maximize the usefulness of the observations.

Acknowledgments. We acknowledge the modeling groups, especially the Program for Climate Model Diagnosis and Intercomparison (PCMDI) and the WCRP Working Group on Coupled Modeling (WGCM), for their roles in making available the WCRP CMIP3 multimodel dataset. Invaluable consultation as to the inner workings of the precipitation schemes employed in the used in this study was provided by Lynne DiPretore of Rutgers University, and we appreciate the excellent comments from two reviewers. Support for this research was provided by the Department of Energy's (DOE) Office of Science, under Grant DE-FG02-08ER64531. Drs. Ashley Williamson and Wanda Ferrell of the DOE Office of Science have been highly supportive of this work. Data were obtained from the Atmospheric Radiation Measurement (ARM) program sponsored by the DOE, Office of Science, Office of Biological and Environmental Research, Climate and Environmental Sciences Division. Our work is dedicated to the fond memory of Dr. Anthony Slingo.

APPENDIX

Calculating the CRF and CRE from AMF and GERB Measurements

The methods used to determine the clear-sky SW and LW radiative fluxes from the AMF1 and GERB measurements used to compute the CRE are described in this appendix. These clear-sky fluxes represent the conditions that would have been observed in a cloudy environment if the clouds were removed. The method is similar to the one proposed by Cess et al. (1995) for SW fluxes and Ghate et al. (2009) for LW fluxes.

Determining the surface clear-sky downwelling SW flux when scattered clouds are present and the dataset is extensive is best accomplished in this region by plotting the surface downwelling SW flux and TOA upwelling SW flux against the cosine of the solar zenith angle for each month of the year. The relevant plots for the months of February and August 2006 are shown in the top rows of Figs. A1 and A2. Clear-sky observations from TOA form a linear lower boundary as a function of solar zenith angle when skies are clear because the albedo of the clouds does not contribute to the upwelling flux. This line is the clear-sky flux that is subtracted from all-sky observations to compute the CRF and CRE.

Clear-sky measurements, made at the surface, cluster along a line representing the maximum observed SW flux as a function of solar zenith angle, and this line is an estimate of the clear-sky SW flux that can be subtracted from the all-sky data, thereby producing an estimate of the CRF. These clear-sky estimates also quantify the impacts of dust, thereby negating their impact in the computation of CRF. The initial fitting procedure used in Cess et al. (1995) is used in this analysis. The data points shown are 15-min averages of 1-min resolution SW radiation measurements, and from these 15-min averages we select the largest 10% of measurements in angular bins of width 0.1 ($\delta\cos\theta = 0.1$) and compute the average of these values. The resulting averages are assigned to the angle at the bin center

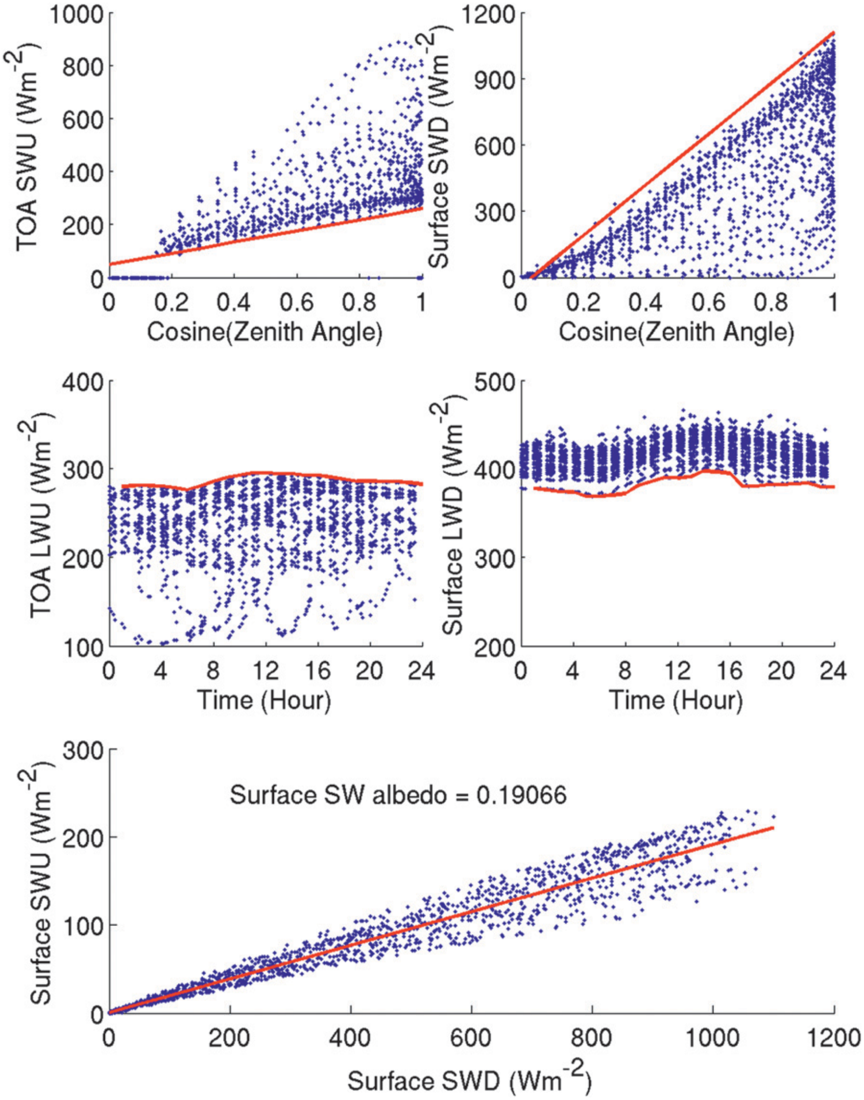

FIG. A1. Data from August 2006 showing (top) TOA SW upwelling and surface SW downwelling clear-sky radiation vs cosine (solar zenith angle), (middle) TOA LW upwelling and surface LW downwelling vs time of day, and (bottom) surface SW downwelling vs surface SW upwelling.

(bin center − 0.05 → bin center + 0.05) and, like Cess et al., irradiances with solar zenith angles higher than 72° ($\cos\theta < 0.3$) are not used. Remaining data points are subject to a linear fit. The fitted line lies above the perceptible linear clustering of points and passes through points that lie above this clustering. This leads to the impression that we have fit our line to data points that exhibit SW enhancement (Berg et al. 2011). Actually, the line lies above the clustering because the highest 10% of the observations in the angular bins are selected, which have a width of 0.1. The largest values of SW downwelling irradiance in these angular bins will be observed at larger values of $\cos\theta$ (i.e., lower zenith angle), which tends to bias the average in each bin to the high side in the midranges of $\cos\theta$. Unfortunately, reducing the width of the angular bins decreases the number of available points and leads to an increase in the uncertainty of the fit, so there is a trade-off. Notably, the line represents the data points at low zenith angle with good integrity, which is important because these points represent the highest energy input to the surface.

Shortcomings of this SW fitting technique were realized by Cess et al. (1995), and they resorted to computing a second quantity, given by

$$-\frac{d(\text{TOA albedo})}{d\left(\dfrac{\text{TOA insolation}}{\text{surface insolation}}\right)}$$

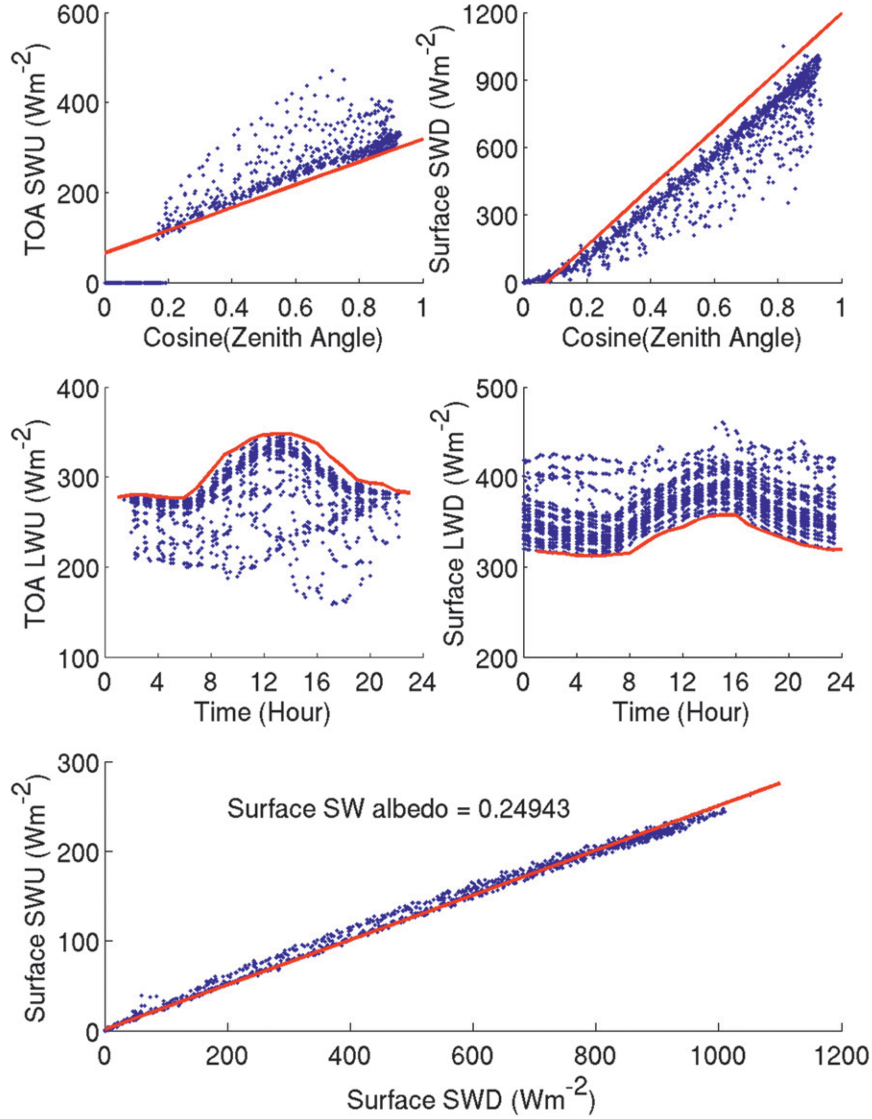

FIG. A2. As in Fig. A1 but for February 2006.

and identifying clear-sky points as being present in a certain portion of the resulting phase space. While this technique is a viable alternative for surface measurements collected in regions where aerosol loading is relatively small, as are the cases considered in Cess et al., it is not likely to succeed in a region like West Africa where aerosols contribute significantly to the TOA albedo and reduce the surface insolation. The approach taken in the current study, while probably not perfect, seems to be the best compromise for this particular region. Interestingly, if we were to assume that the clear-sky SW radiation lies at the upper edge of the clustering of points, the observed CRE would be significantly larger than the values that we compute and would disagree even more with the GCMs. Notwithstanding, an interesting and fundamental future science question involves the techniques used to identify clear skies in regions with heavy aerosol loads.

Measuring the surface LW CRF involves a similar procedure, but time of day replaces the cosine of the solar zenith angle (middle rows of Figs. A1 and A2). Clear skies are assumed when the LW upwelling flux at the TOA is a maximum, indicating the maximum amount of LW loss to space. Conversely, clear skies are associated with minimum downwelling LW radiation at the surface. Fits to these boundaries enable the calculation of the surface and TOA LW CRF.

To calculate the clear-sky upwelling SW fluxes, the surface SW albedo for each month was calculated using the best fit between downwelling SW flux and upwelling SW flux at the surface. From the albedo (slope of the fit), and using the clear-sky downwelling SW flux at the surface, clear-sky upwelling SW flux at the surface was calculated. Examples of these scatterplots for the months of August and February are shown in the bottom panels of Figs. A1 and A2. The albedo was 0.19 during August and 0.25 during February, in excellent agreement with the values computed in McFarlane et al. (2009), which were 0.20 and 0.25, respectively. Similar to the GCMs, the upwelling LW flux at the surface is kept the same for all-sky and clear-sky conditions.

REFERENCES

Allan, R. P., A. Slingo, S. F. Milton, and M. E. Brooks, 2007: Evaluation of the Met Office Global Forecast Model using Geostationary Earth Radiation Budget (GERB) data. *Quart. J. Roy. Meteor. Soc.,* **133,** 1993–2010.

Augustine, J. A., J. J. DeLuisi, and C. N. Long, 2000: SURFRAD—A national surface radiation budget network for atmospheric research. *Bull. Amer. Meteor. Soc.,* **81,** 2341–2357.

Berg, L. K., E. I. Kassianov, C. N. Long, and D. L. Mills, 2011: Surface summertime radiative forcing by shallow cumuli at the Atmospheric Radiation Measurement Southern Great Plains site. *J. Geophys. Res.,* **116,** D01202, doi:10.1029/2010JD014593.

Cess, R. D., and Coauthors, 1995: Absorption of solar radiation by clouds: Observation versus models. *Science,* **267,** 496–499.

Clerbaux, N., S. Dewitte, C. Bertrand, D. Caprion, B. Depaepe, L. Gonzalez, A. Ipe, and J. Russell, 2008a: Unfiltering of the Geostationary Earth Radiation Budget (GERB) data. Part I: Shortwave radiation. *J. Atmos. Oceanic Technol.,* **25,** 1087–1105.

——, ——, ——, ——, ——, ——, ——, and ——, 2008b: Unfiltering of the Geostationary Earth Radiation Budget (GERB) data. Part II: Longwave radiation. *J. Atmos. Oceanic Technol.,* **25,** 1106–1117.

Collins, W. D., and Coauthors, 2006: The community climate system model version 3 (CCSM3). *J. Climate,* **19,** 2122–2143.

Delworth, T. L., and Coauthors, 2006: GFDL's CM2 global coupled climate models. Part I: Formulation and simulation characteristics. *J. Climate,* **19,** 643–674.

Dewitte, S., L. Gonzalez, N. Clerbaux, A. Ipe, and C. Bertrand, 2008: The Geostationary Earth Radiation Budget Edition 1 data processing algorithms. *Adv. Space Res.,* **41,** 1906–1913.

Freidenreich, S., and V. Ramaswamy, 2011: Analysis of the biases in the downward shortwave surface flux in the GFDL CM2.1 general circulation model. *J. Geophys. Res.,* **116,** D08208, doi:10.1029/2010JD014930.

Ghate, V. P., B. A. Albrecht, C. W. Fairall, and R. A. Weller, 2009: Climatology of surface meteorology, surface fluxes, cloud fraction, and radiative forcing over the southeast Pacific from buoy observations. *J. Climate,* **22,** 5527–5540.

Gu, G., and R. F. Adler, 2004: Seasonal evolution and variability associated with the West African monsoon system. *J. Climate,* **17,** 3364–3377.

Harries, J. E., and Coauthors, 2005: The Geostationary Earth Radiation Budget project. *Bull. Amer. Meteor. Soc.,* **86,** 945–960.

Huang, J., C. Zhang, and J. M. Prospero, 2009: African aerosol and large-scale precipitation variability over West Africa. *Environ. Res. Lett.,* **4,** 015006, doi:10.1088/1748-9326/4/1/015006.

Kandji, S., L. Verchot, and J. Mackensen, 2006: Climate change and variability in the Sahel region: Impacts and adaptation strategies in the agricultural sector. U.N. Environmental Programme and World Agroforestry Centre Tech. Rep., 48 pp. [Available online at http://www.unep.org/Themes/Freshwater/Documents/pdf/ClimateChangeSahelCombine.pdf.]

Kollias, P., M. A. Miller, K. L. Johnson, M. P. Jensen, and D. T. Troyan, 2009: Cloud, thermodynamic, and precipitation observations in West Africa during 2006. *J. Geophys. Res.,* **114,** D00E08, doi:10.1029/2008JD010641.

Lamb, P. J., 1986: Waiting for rain. *Sciences,* **26** (3), 30–35.

——, R. A. Peppler, and S. Hastenrath, 1986: Interannual variability in the tropical Atlantic. *Nature,* **322,** 238–240.

Lavender, S., and A. J. Matthews, 2009: Response of the West African monsoon to the Madden–Julian oscillation. *J. Climate,* **22,** 4097–4116.

Lélé, M. I., and P. J. Lamb, 2010: Variability of the intertropical front (ITF) and rainfall over the West African Sudan–Sahel zone. *J. Climate,* **23,** 3984–4004.

Loeb, N., K. Priestley, D. Kratz, E. Geier, R. Green, B. Wielicki, P. Hinton, and S. Nolan, 2001: Determination of unfiltered radiances from the Clouds and the Earth's Radiant Energy System instrument. *J. Appl. Meteor.,* **40,** 822–835.

Maloney, E. D., and J. Shaman, 2008: Intraseasonal variability of the West African monsoon and Atlantic ITCZ. *J. Climate,* **21,** 2898–2917.

Martin, G. M., M. A. Ringer, V. D. Pope, A. Jones, C. Dearden, and T. J. Hinton, 2006: The physical properties of the atmosphere in the new Hadley Centre Global Environmental Model, HadGEM1. Part I: Model description and global climatology. *J. Climate,* **19,** 1274–1301.

Matthews, A. J., 2004: Intraseasonal variability over tropical Africa during northern summer. *J. Climate,* **17,** 2427–2440.

McFarlane, S. A., J. H. Mather, T. P. Ackerman, and Z. Liu, 2008: Effect of clouds on the calculated vertical distribution of shortwave absorption in the tropics. *J. Geophys. Res.,* **113,** D18203, doi:10.1029/2008JD009791.

——, E. I. Kassianov, J. Barnard, C. Flynn, and T. P Ackerman, 2009: Surface shortwave aerosol radiative forcing during the Atmospheric Radiation Measurement Mobile Facility deployment in Niamey, Niger. *J. Geophys. Res.,* **114,** D00E06, doi:10.1029/2008JD010491.

Meehl, G. A., C. Covey, T. Delworth, M. Latif, B. McAvaney, J. F. B. Mitchell, R. J. Stouffer, and K. E. Taylor, 2007: The WCRP CMIP3 multimodel dataset: A new era in climate change research. *Bull. Amer. Meteor. Soc.,* **88,** 1383–1394.

Miller, M. A., and A. Slingo, 2007: The ARM Mobile Facility and its first international deployment: Measuring radiative flux divergence in West Africa. *Bull. Amer. Meteor. Soc.,* **88,** 1229–1244.

Parding, K., L. M. Hinkelman, T. P. Ackerman, and S. McFarlane, 2011: Shortwave absorptance in a tropical cloudy atmosphere: Reconciling calculations and observations. *J. Geophys. Res.,* **116,** D18203, doi:10.1029/2011JD015639.

Pohl, B., S. Janicot, B. Fontaine, and R. Marteau, 2009: Implications of the Madden–Julian oscillation in the 40-day variability of the West African monsoon. *J. Climate,* **22,** 3769–3785.

Ramanathan, V., R. D. Cess, E. F. Harrison, P. Minnis, and B. R. Barkstrom, 1989: Cloud-radiative forcing and climate: Results from the Earth Radiation Budget Experiment. *Science,* **243,** 57–63.

Revercomb, H., and Coauthors, 2003: The ARM program's water vapor intensive observation periods. *Bull. Amer. Meteor. Soc.,* **84,** 217–236.

Rossow, W. B., and R. A. Schiffer, 1991: ISCCP cloud data products. *Bull. Amer. Meteor. Soc.,* **72,** 2–20.

——, and E. N. Dueñas, 2004: The International Satellite Cloud Climatology Project (ISCCP) web site: An online resource for research. *Bull. Amer. Meteor. Soc.,* **85,** 167–172.

Ruiz-Barradas, A., and S. Nigam, 2006: IPCC's twentieth-century climate simulations: Varied representation of North American hydroclimate variability. *J. Climate,* **19,** 4041–4058.

Schmetz, J., P. Pili, S. Tjemkes, D. Just, J. Kerkmann, S. Rota, and A. Ratier, 2002: An introduction to Meteosat Second Generation (MSG). *Bull. Amer. Meteor. Soc.,* **83,** 977–992.

Schmidt, G. A., and Coauthors, 2006: Present-day atmospheric simulations using GISS ModelE: Comparison to in situ, satellite, and reanalysis data. *J. Climate,* **19,** 153–192.

Settle, J. J., N. A. Bharmal, G. J. Robinson, and A. Slingo, 2008: Sampling uncertainties in surface radiation budget calculations in RADAGAST. *J. Geophys. Res.,* **113,** D00E02, doi:10.1029/2008JD010509.

Slingo, A., and Coauthors, 2006: Observations of the impact of a major Saharan dust storm on the atmospheric radiation balance. *Geophys. Res. Lett.,* **33,** L24817, doi:10.1029/2006GL027869.

——, and Coauthors, 2008: Overview of observations from the RADAGAST experiment in Niamey, Niger: Meteorology and thermodynamic variables. *J. Geophys. Res.,* **113,** D00E01, doi:10.1029/2008JD009909.

——, H. E. White, N. A. Bharmal, and G. J. Robinson, 2009: Overview of observations from the RADAGAST experiment in Niamey, Niger: 2. Radiative fluxes and divergences. *J. Geophys. Res.,* **114,** D00E04, doi:10.1029/2008JD010497.

Soden, B. J., A. J. Broccoli, and R. S. Hemler, 2004: On the use of cloud forcing to estimate cloud feedback. *J. Climate,* **17,** 3661–3665.

——, I. M. Held, R. Colman, K. M. Shell, J. T. Kiehl, and C. A. Shields, 2008: Quantifying climate feedback using radiative kernels. *J. Climate,* **21,** 3504–3520.

Stoffel, T., 2005: Solar Infrared Radiation Station (SIRS) handbook. ARM TR-025, Department of Energy, Washington, DC, 29 pp. [Available online at http://www.arm.gov.]

Thorncroft, C. D., and B. J. Hoskins, 1994: An idealized study of African easterly waves. Part I: A linear view. *Quart. J. Roy. Meteor. Soc.,* **120,** 953–982.

Yoshioka, M., N. Mahowald, A. J. Conley, W. D. Collins, D. W. Fillmore, C. S. Zender, and D. Coleman, 2007: Impact of desert dust radiative forcing on Sahel precipitation: Relative importance of dust compared to sea surface temperature variations, vegetation changes, and greenhouse gas warming. *J. Climate,* **20,** 1445–1467.